Measurement report: Characteristics of airborne black carbon-containing particles during the 2021 summer COVID-19 lockdown in Yangzhou, China

Yuan Dai[1,2,3], Junfeng Wang[1,2], Houjun Wang[3], Shijie Cui[1,2], Yunjiang Zhang[1,2], Haiwei Li[1,2], Yun Wu[1,2], Ming Wang[1,2], Eleonora Aruffo[5], Xinlei Ge[1,2,4*]

[1]Jiangsu Key Laboratory of Atmospheric Environment Monitoring and Pollution Control, Collaborative Innovation Center of Atmospheric Environment and Equipment Technology, School of Environmental Science and Engineering, Nanjing University of Information Science and Technology, Nanjing 210044, China
[2]International Joint Laboratory on Climate and Environment Change (ILCEC), Nanjing University of Information Science and Technology, 210044 Nanjing, China
[3]Yangzhou Environmental Monitoring Center, Yangzhou 225009, China
[4]School of Environment and Energy Engineering, Anhui Jianzhu University, Hefei 230601, China
[5]Department of Advanced Technologies in Medicine & Dentistry, University "G. d'Annunzio" of Chieti-Pescara; Center for Advanced Studies and Technology-CAST, Chieti 66100, Italy

Correspondence: Xinlei Ge (caxinra@163.com)

Abstract

Black carbon-containing particles (BCc) are ubiquitous in ambient air, significantly contributing to particulate matter (PM) pollution. The unexpected outbreak of the COVID-19 pandemic in the summer of 2021 prompted a localized and prolonged lockdown in Yangzhou City, situated in the Yangtze River Delta, China. This lockdown led to significantly altering in local anthropogenic emissions, while neighboring cities continued regular operations, providing a unique opportunity for the investigation of BCc characteristics influenced by varying emission conditions. Single particle aerosol mass spectrometer (SPA-MS) analysis revealed a notable decrease in the proportion of freshly emitted BCc during the lockdown period (LD). However, $PM_{2.5}$ concentrations remained relatively unchanged, with an observed increase in the proportion of aged BCc during LD compared to the period before the lockdown (BLD). The study also underscored the significant role of regional transport in $PM_{2.5}$ pollution during the campaign. Moreover, reactive trace gases (e.g., NO_x, SO_2, and VOCs) could form thick coatings on pre-existing particles likely via enhanced heterogeneous hydrolysis under high relative humidity (RH) as well, resulting in significant BCc particle growth (~600 nm), as well as $PM_{2.5}$, during LD. Our study highlights that short-term, strict local emission controls may not effectively reduce PM pollution due to the complex production and transmission characteristics of BCc and the non-linear responses of $PM_{2.5}$ to its precursors. Achieving further effective $PM_{2.5}$ reduction mandates a focus on nuanced control of BCc and necessitates a comprehensive and extensive approach with a regionally coordinated and balanced control strategy through joint regulation.

1. Introduction

China has implemented long-term clean air measures to cut down anthropogenic emissions and improve air quality (Ge et al., 2020), resulting in a nationwide reduction of average fine particulate matter ($PM_{2.5}$, aerodynamic diameter ≤ 2.5 μm) level from 50 μg m^{-3} in 2015 to 30 μg m^{-3} in 2020 (Zhou et al., 2022). However, this $PM_{2.5}$ concentration remains significantly higher than the new World Health Organization (WHO) guideline value of 5 μg m^{-3} (*WHO Global Air Quality Guidelines*, 2021). Black carbon (BC) is a ubiquitous component of aerosols, typically constituting a small proportion (5~10%) of $PM_{2.5}$ in the atmosphere (Chen et al., 2020). However, freshly emitted BC evolves into BC-containing particles (BCc) by undergoing atmospheric aging, contributing to a rise in the total mass of $PM_{2.5}$ through processes of coating or embedding by other materials (Bond and Bergstrom, 2006; Peng et al., 2016). The number and mass fraction of BCc can excess 60% and 50% of $PM_{2.5}$, respectively, emphasizing the significant role of BC in elevating the mass concentration of particulate matter (PM) (Sun et al., 2022; Xie et al., 2020; Chen et al., 2020).

The atmospheric aging of BCc involves intricate chemical and physical transformations that influence their mixing state, morphology, hygroscopicity, and optical properties, all of which have profound implications for climate and human health (Bond et al., 2013; Ramanathan et al., 2008). For example, freshly emitted BC particles are initially hydrophobic but possess a porous surface structure that facilitates the internal or external mixing with co-emitted primary organic/inorganic and secondary materials that are associated with BC (Cheng et al., 2012; Li et al., 2020). On the other hand, BCc undergoes continually aging processes, including the condensation of low-volatility vapors (Li et al., 2022), coagulation with preexisting aerosols (Kondo et al., 2011), and heterogeneous oxidation with gaseous pollutants (Zhang et al., 2024). This alteration may affect the coating thickness, morphology, size distribution, and hygroscopicity of BCc, thereby impacting their climate forcing as well as atmospheric lifetime (Luo et al., 2022; Taylor et al., 2014). High loading of atmospheric BCc could also depress the development of the planetary boundary layer and exacerbate PM pollution episodes (Huang et al., 2018). BCc characteristics are influenced by various combustion sources and emission conditions, including local industrial burning, vehicle exhausts, residential coal burning, and biomass burning (Li et al., 2020; Sedlacek et al., 2022; Zhang et al., 2018), as well as long-range transport from other regions (Adachi et al., 2014; Zhang et al., 2021). Those diverse conditions complicate the development of parameterizations of BCc properties, the insufficient understanding of complex emission sources, aging processes, and physical properties of BCc, hampering the effectiveness of air quality remediation (Cappa et al., 2019; Kahnert, 2010; Sun et al., 2021).

Studies on the effects of large-scale and short-term stringent emission control events on air quality in China have been widely deployed, e.g., the 2008 Beijing Olympic Games

(Wang et al., 2010; Zhou et al., 2010), the 2015 Asia-Pacific Economic Cooperation (APEC) (Zhu et al., 2015), the 2014 Nanjing Youth Olympic Games (Wang et al., 2022) and the national COVID-19 lockdown in 2020 winter (Huang et al., 2021; Le et al., 2020; L. Li et al., 2020; Wang et al., 2020). Previous studies extensively investigated air pollutant variations during the COVID-19 lockdown in the winter of 2020 across different regions of the world. Stringent restrictions on industrial and vehicular activities have resulted in significant reductions in gaseous pollutants and particulate matter, not only in megacities (Chen et al., 2020; Jeong et al., 2022; Sun et al., 2020) but also in middle-sized cities (Clemente et al., 2022; Wang et al., 2021; Xu et al., 2020) and rural areas (Cui et al., 2021, 2020; Jain et al., 2021). Compared to the decreasing trends observed in most cities worldwide, the level of $PM_{2.5}$ in Shanghai (Chang et al., 2020), Hohhot (Zhou et al., 2022), and the Northeast of China Plain (Nie et al., 2021) increased unexpectedly. These observations reveal the complex aerosol chemistry of $PM_{2.5}$ comprising primary and secondary components. The reduction of primary pollutants during lockdown resulted in a shift towards a higher proportion of secondary aerosols, including inorganic and organic species, exhibiting a non-linear response to emission changes (Zhang et al., 2021). Furthermore, some studies suggested that the increase in secondary aerosols during lockdown is due to the enhanced atmospheric oxidative capacity resulting from the rise in ozone levels (Wang et al., 2021), unfavorable meteorological conditions (Chien et al., 2022; Sulaymon et al., 2021a), changes of local and regional emission sources (Feng et al., 2022). However, most previous studies focused on lockdown events during the cold seasons, and studies on summer lockdown events in China were very limited.

Yangzhou is located in the central region of the Yangtze River Delta (YRD), at the junction of the Yangtze River and, the Beijing-Hangzhou Grand Canal, which serves as a prominent economic city, industrial-intensive area, and highly active inland shipping node in East China. Due to the complex emissions and feedback with the East Asian monsoons (Ding et al., 2019), this region is susceptible to anthropogenic aerosols, especially BCc originating from chemical, steelmaking, coal-fired, petrochemical enterprises, and transportation, etc. Extensive studies have investigated the responses of atmospheric pollutants to emission changes during the COVID-19 lockdown measures in the YRD (Chen et al., 2021; Li et al., 2020; Qin et al., 2021; Zhang et al., 2022). However, the key chemical and physical processes specifically responsible for the BCc in this region are still unclear. During the summer of 2021, Yangzhou experienced a resurgence of COVID-19 with over 500 confirmed cases. In response, stringent public health measures were imposed from July 29th to September 10th, including the closure of public transport, and suspension of non-essential industrial plants, restaurants, shopping malls, and entertainment clubs. People were also mandated to quarantine at home. Consequently, Yangzhou experienced a significant decline in transportation and industrial energy consumption, dropping by nearly 46% and 25%, respectively, compared to the same period in 2020 (www.yangzhou.gov.cn),

implying a substantial reduction in human activity and primary emissions. Unlike the nationwide COVID-19 lockdown in China during the cold season of 2020 (Le et al., 2020; Sulaymon et al., 2021b), the summer lockdown in Yangzhou was more localized but protracted, significantly altering local anthropogenic emissions while neighboring cities maintained regular operations, which provides a unique opportunity to explore and compare the diverse mixing states and, the aging process of BCc in different anthropogenic emission conditions in summer. Here we report the chemical compositions and aging characteristics of airborne BCc in YRD. Our investigation involved a combination of ground measurements, spaceborne observations, and mass spectrometric analysis conducted during the COVID-19 lockdown in the summer of 2021 in Yangzhou. Additionally, we employed potential source contribution function (PSCF) analysis to investigate the air pollution patterns in the YRD.

2. Methods

2.1 Sampling site and instruments

The in-situ online measurements were conducted at a rooftop laboratory 20 m above ground located in a national air quality monitoring station, Yangzhou Environmental Monitoring Center (32.41ºN, 119.40ºE), Yangzhou, China (**Figure 1**). This sampling site is a typical urban site surrounded by residential areas, arterial roads, parks, restaurants, and shopping centers. In this study, the measurement period was divided into three phases: the before-lockdown period (BLD: 30 June to 28 July 2021), the lockdown period (LD: 29 July to 9 September 2021), and the after-lockdown period (ALD: 10 September to 7 October 2021) (**Figure 2**).

A single-particle aerosol mass spectrometer (SPA-MS, Hexin Analytical Instrument Co., Ltd., China) was deployed during the field campaign to obtain the chemical composition, size distribution, and mixing state of individual $PM_{2.5}$ particles. A cyclone with a 2.5 μm cutpoint (Model URG-2000-30ED) and a Nafion dryer is equipped in front of the sampling inlet. Individual particles are introduced into the SPA-MS through a critical orifice at a flow rate of 3 L min^{-1}. The vacuum aerodynamic diameters (D_{va}) are determined using the velocities derived from two continuous laser beams (diode Nd: YAG, 532 nm) spaced 6 cm apart. Subsequently, these particles are desorbed and ionized by a downstream pulsed laser (266 nm), and ion fragments are generated and measured by a Z-shaped bipolar time-of-flight mass spectrometer. A more detailed description of SPA-MS can be found in previous studies (Li et al., 2011).

$PM_{2.5}$ mass concentration was measured by a particulate matter monitor (XHPM2000E, Xianhe, China). Nitrogen oxides (NO_x = NO + NO_2), SO_2, and ozone (O_3) concentrations were detected with a set of Thermo Fisher Scientific instruments (Models 42i, 43i, and 49i). The concentrations of 103 volatile organic compounds (VOCs) in ambient air, comprising 57 ozone precursors (PAMS), 12 aldehydes and ketones, and 34 toxic organics (TO15), were continuously monitored at hourly intervals

using an online device (TH-300B, Tianhong, China). Meteorological parameters, including ambient temperature (T), relative humidity (RH), wind direction (WD), and wind speed (WS) were observed synchronously using an automatic weather instrument (WXT530, Vaisala, Finland). Precipitation (PCP) data was obtained from the Yangzhou Meteorological Bureau. All online data presented in this paper were hourly averaged at local time (Beijing time, UTC+8).

2.2 Data analysis

2.2.1 Satellite Product

In this study, we utilized the Copernicus Atmosphere Monitoring Service (CAMS) Global Near-Real-Time dataset (available at https://developers.google.com/earth-engine/datasets/catalog/ECMWF_CAMS_NRT), acquired from the European Centre for Medium-Range Weather Forecasts (ECMWF), to analyze the distribution of total surface column concentrations of NO_2, SO_2 and surface $PM_{2.5}$ mass concentration. CAMS offers the capacity to continuously monitor the composition of the Earth's atmosphere at global and regional scales since 2016, with a spatial resolution of 44528 meters (Benedetti et al., 2009; Morcrette et al., 2009). The details of the bands of the dataset used in this study are shown in Table S2. We calculated and plotted the averaged 2-dimensional data of ECMWF/CAMS/NRT NO_2, SO_2, and $PM_{2.5}$ during BLD and LD over the region of interest (17.93~54.74 ºN, 71.21~142.23 ºE) using Google Earth Engine (Gorelick et al., 2017). The integration of remote sensing measurements has provided a more comprehensive understanding of the sources and distributions of particle matter and gaseous pollutants facilitating the evaluation of the impact of human activities on air quality.

2.2.2 Geographic Source Analysis

The potential source contribution function (PSCF) analysis, based on the Hybrid Single-Particle Lagrangian Integrated Trajectory (HYSPLIT) model, can be employed to identify regional sources of air pollutants. Before conducting the PSCF analysis, 36 hours of air mass backward trajectories with one-hour resolution at 500 m above ground level were calculated using the wind data from the Global Data Assimilation System (GDAS) provided by the National Oceanic and Atmospheric Administration (NOAA) (Wang et al., 2009). An open-source software MeteoInfo (Wang, 2014) was utilized for the PSCF analysis. The whole study area (110.1~133.4 ºE and 21.3~39.9 ºN) covered by the trajectories was divided into thousands of cells with a spatial resolution of 0.1° × 0.1°. The PSCF was simulated according to the following equation:

$$PSCF_{ij} = \frac{m_{ij}}{n_{ij}} \quad (1)$$

where $PSCF_{ij}$ is the conditional probability that the grid cell (i, j) was a source of the species found in high concentration (Hopke et al., 1993); n_{ij} is the number of all trajectories passing through this grid cell, and m_{ij} is the number of trajectories. In this study, the pollution criterion values for different BCc particle types were set as the 75th

percentile of hourly average number fractions, respectively. To further improve the accuracy of the PSCF analysis and minimize analytical uncertainties, the Weighted PSCF (WPSCF) functions as shown in Equation (2~3) were applied (Polissar et al., 1999). The weight (W_{ij}) for each grid cell was determined based on the number of trajectory endpoints (n_{ij}) as follows:

$$WPSCF_{ij} = W_{ij} \times PSCF_{ij} \quad (2)$$

$$W_{ij} = \begin{cases} 1.00 & n_{ij} > 3n_{ave} \\ 0.70 & 1.5n_{ave} < n_{ij} \leq 3n_{ave} \\ 0.40 & n_{ave} < n_{ij} \leq 1.5n_{ave} \\ 0.17 & n_{ij} \leq n_{ave} \end{cases} \quad (3)$$

Here, n_{ave} is the average number of trajectory endpoints of each grid.

2.2.3 SPA-MS Data Analysis

In total, 1649574 particles were analyzed during the entire observation period. The size and chemical composition of single particles were analyzed using the Computational Continuation Core (COCO V1.4) toolkit in MATLAB 2022 (The MathWorks, Inc.). Our focus was on BCc, which was identified based on the relative peak area (RPA) of carbon ion clusters ($C_n^{\pm}$, n = 1, 2, 3, …), with a threshold of 0.05 (Zhang et al., 2021). An adaptive resonance theory-based neural network algorithm (ART-2a) was applied to classify the measured individual particles based on the presence and intensity of ion peaks, with a vigilance factor of 0.75, a learning rate of 0.05, and 20 iterations (Song et al., 1999).

3. Results and discussion

3.1 Field observations

Figure 2 presents the temporal variations of meteorological parameters, $PM_{2.5}$, NO_x, and SO_2 concentrations. Notably, significantly reductions in $PM_{2.5}$, NO_x, and SO_2 were observed at the end of BLD due to a high precipitation event, with a peak hourly precipitation reaching 37 mm, and the data collected during this event were excluded from the analysis. During BLD, the mean temperature (*T*) was 28±3 ℃, the total precipitation was 221 mm, with an average relative humidity (RH) of 83±12%. The prevailing winds originated from the south and southeast, with a mean wind speed (WS) of 3.3±1.2 m s^{-1}. In comparison, LD shows a decline in temperature to 27±2 ℃ and WS to 2.3±1.0 m s^{-1}, but an increase in RH to 87±11% and a reduction in total precipitation to 86 mm. **Figure S2b and c** present uniform distributions of RH and boundary-layer height (BLH) across the YRD during LD. These regional meteorological conditions and the effective removal of the pollutants accumulated at the end of BLD facilitated the investigation of BCc regional transport in YRD. During ALD, the temperature declined further to 25±3 ℃, WS increased to 3.3±1.5 m s^{-1}, and total precipitation dropped to 27 mm with a lower RH of 77±14%.

During LD, strict measures resulted in notably lower surface concentrations of $PM_{2.5}$ (20.3 μg m^{-3}), NO_x (16.8 μg m^{-3}) and TVOC (55.9 μg m^{-3}) compared to BLD and ALD. Conversely, the surface O_3 concentration showed an increase of 18.4 μg m^{-3} (28%) during LD relative to BLD. The reduction of fresh NO emission alleviates O_3 titration (Steinfeld, 1998) could be an explanation. Analysis from **Figure S3** indicates that the O_3 level is higher than those of neighboring cities in the YRD, suggesting higher local atmospheric oxidation capacity during LD. However, the average concentrations of $PM_{2.5}$ (20.6 vs. 20.3 μg m^{-3}), SO_2 (9.1 vs. 9.2 μg m^{-3}) and CO (0.61 vs. 0.62 mg m^{-3}) were comparable during both BLD and LD (**Figure 3**).

After LD, social activities gradually resumed in Yangzhou City, leading to an apparent increase in all observed pollutants during the ALD period. For instance, there were relative increases of 66% for NO_x, 19% for SO_2, 36% for TVOC, 14% for O_3, 32% for $PM_{2.5,}$ and 16% for CO from LD to ALD, respectively (**Figure 3**). Given that both BC and CO are byproducts of incomplete combustion of carbon-containing fuels (Wang et al., 2015), and the high correlation between BC and CO (Zhou et al., 2009), it is plausible to infer that the primary emission source of BC during LD differed from those during ALD. This change likely reflects the shift in combustion practices and fuel usage patterns as economic activities restarted during ALD.

Satellite-retrieved $PM_{2.5}$, NO_2, and SO_2 data over the entire region of eastern China were also investigated, and results show that these pollutants were predominantly concentrated in Shanghai and its neighboring cities, including Yangzhou, during both BLD and LD (**Figure S4**). **Figure 4** presents regional fractional changes of mean $PM_{2.5}$, NO_2, and SO_2 concentrations from the BLD to LD periods in YRD, all showing an increase of 29%, 6%, and 14%, respectively. In comparison, Yangzhou city experienced lower increases in these air pollutants, with slight changes of 6%, -18%, and -4% for $PM_{2.5}$, NO_2, and SO_2, respectively. The implication is that, even though local primary emissions, such as NO_2, and SO_2, were reduced substantially during LD, they still could be affected by regional transport. Furthermore, as depicted in **Figure S3**, the concentrations of NO_2 in major cities of the YRD were more than twice higher than in Yangzhou during LD, confirming a relatively lower local primary emissions due to the stringent lockdown. However, the higher level of SO_2 in Yangzhou during LD may be attributed to the nearby power stations along the Yangtze River, which were not impacted by the lockdown measures.

3.2 Chemical composition and size distribution of individual BCc

Based on the SPA-MS analysis, a total of 1068362 BCc was collected during the whole study period. The BCc accounted for 59%, 69%, and 57% of the total number of measured particles in the BLD, LD, and ALD periods, respectively. **Figure 5** shows the normalized average mass spectra of BCc during three periods. Ion height in each spectrum reflects the number fraction of the detected BCc with the corresponding ion

to the total BCc, while colors represent peak area ranges of detected ions. BCc in BLD, LD, and ALD shown similar mass spectra at *m/z* < 100, with common peaks including carbon ion clusters ($C_n^{\pm}$, n = 1~7), m/z 27$[C_2H_3]^+$, 37$[C_3H]^+$, 43$[C_2H_3O]^+$, 51$[C_4H_3]^+$, 63$[C_5H_3]^+$, 46$[NO_2]^-$, 62$[NO_3]^-$, and 97$[HSO_4]^-$. However, the abundance of large *m/z* carbon ions ($C_n^{\pm}$, n > 7) in both BLD and ALD periods was 1.5 times higher than that in the LD. Previous studies have indicated that high-mass carbon ions may be linked to traffic emissions, particularly those from diesel trucks(Xie et al., 2020; Liu et al., 2019), and the observed reduction in such ions during LD suggests a decrease in local vehicle emissions. This trend is also consistent with the changes observed in aromatic compounds, e.g. m/z 119$[C_9H_{11}]^+$.

Further, BCc was classified into 12 types based on the differences in chemical features and temporal variations, as shown in **Table S1**. Fresh BC particles (BC-fresh) are those freshly emitted without undergoing significant atmospheric processing (Ding et al., 2021). Five types of BC-fresh particles were identified according to their ion markers: (i) BC-pure is dominated by carbon clusters ($C_n^{\pm}$) with minor ion signals of inorganic species, such as m/z 46$[NO_2]^-$ and m/z 97$[HSO_4]^-$ from nitrate and sulfate, respectively (Xie et al., 2020); (ii) BCc from biomass burning (BB) are characterized by ion signals at *m/z* 39$[K]^+$, 45$[CHO_2]^-$, 59$[C_2H_3O_2]^-$, and 73$[C_3H_5O_2]^-$, with a relative peak area (RPA) more than 0.5 (Silva et al., 1999); (iii) coal combustion BCc (CC) typically include small carbon clusters ($C_n^{\pm}$, n = 1~4), metal elements (e.g., m/z 7$[Li]^+$, 23$[Na]^+$, 27$[Al]^+$, 56$[Fe]^+$, 63$[Cu]^+$ and 206/207/208$[Pb]^+$), and organic carbon (38$[C_3H_2]^+$, 43$[C_2H_3O]^+$) peaks in the positive mass spectrum, while the strong signals of secondary inorganic species (46$[NO_2]^-$, 43$[AlO]^-$, 62$[NO_3]^-$, 80$[SO_3]^-$, 97$[HSO_4]^-$) in the negative ion mode suggest that CC particles were long-distance transported or more processed (Zhang et al., 2022; Zhang et al., 2009); (iv) particles from vehicle emission (VE) are characterized by the presence of ion signals at *m/z* 40$[Ca]^+$, 51$[V]^+$, 55$[Mn]^+$, 67$[VO]^+$, 46$[NO_2]^-$, 62$[NO_3]^-$, and 79$[PO_3]^-$, as well as high loadings of organic carbon (41$[C_3H_5]^+$, 43$[C_2H_3O]^+$) and carbon clusters ($C_n^{\pm}$, n = 1~4) ion peaks (Yang et al., 2017); (v) BCc that are internally mixed with more than one type (BB, CC, and VE) are categorized as Mix type (Sun et al., 2022).

Aged BC particles, denote as BC-aged, undergo a series of chemical reactions and physical transformations. These processes typically lead to changes in their morphology, hygroscopicity, and optical properties as they are coated with other materials (He et al., 2015). Six types of BCc are classified as BC-aged and are further grouped into BCOC and BC-SNA, depending on whether they contain mainly organic carbon (OC) or sulfate/nitrate/ammonium (SNA). First, BCOC types indicate BC-aged particles that are internally mixed with OC. These particles are characterized by the presence of carbon clusters ($C_n^{\pm}$) and $C_nH_m^+$ ions (n = 1~6, m = 1~3) in positive mass spectra (Xie et al., 2020). On the other hand, BC-aged particles that do not mix with OC are named BC-SNA indicating the mix with secondary inorganic species. Additionally, BCOC

particles with negative mass spectra dominated by nitrate ions ($46[NO_2]^-$ and $62[NO_3]^-$) or sulfate ions ($97[HSO_4]^-$) are referred to as BCOC-N or BCOC-S, respectively; otherwise, BCOC particles showing similar peak areas of nitrate and sulfate are named BCOC-SN. The BC-SNA particles are further categorized as BC-N, BC-S, and BC-SN based on similar principles. Note the remaining particles that cannot be classified into either BC-fresh or BC-aged ones are denoted as BC-other. More details of BCc particle types are shown in **Table S1** and **Figure S1** in the Supplement.

During BLD, the average number fraction of BC-fresh particles was 36% with sizes mainly concentrated at 500 nm, similar to the mode size of BC-aged particles was 520 nm (**Figures 6**). The predominant BCc types during BLD were BCOC-S and BC-S (24% and 12% by number), likely because sulfate was removed less efficiently than organic matter (OM) and NO_3 by heavy precipitation, especially during the warm seasons (Isokääntäet al., 2022). As shown in **Figures 6c and d**, the peak size of BC-SNA was larger than that of BCOC in all periods, indicating that organics coated BCc generally had a relatively thin coating compared to those coated by secondary inorganic species, which is consistent with previous studies (Sun et al., 2016; Wang et al., 2019).

During the transition from BLD to LD, heavy and continuous precipitation occurred from July 25th to July 28th (the eve of lockdown), resulting in the removal of a majority of the pollutants ($PM_{2.5}$: 4 μg m^{-3}, O_3: 35 μg m^{-3}, NO_x: 8 μg m^{-3}). Following this environmental clearance, strict lockdown measures were implemented, resulting in a drastic reduction in primary emissions. As a result, the number fraction of BC-fresh particles significantly decreased from 37% to 28% and that of VE-type particles dropped from 12% to 3% (by number). Expectedly, with the decrease in NO_x, an obvious enhancement of O_3 was observed during LD (**Figure 3**). According to previous studies (Huang et al., 2021; Laughner et al., 2021), large reduction of NO_x may promote the formation of O_3 under a VOC-limited regime and enhance the oxidation capacity of the local atmosphere, which may promote the number fraction of BC-aged particles increased from 64% in the BLD to 72% in LD (**Figure 7a**), indicating the lockdown could accelerate aging of BCc through complicated chemical reactions and/or physical coagulation. Additionally, the most abundant type of BCc changed from BCOC-S (24% by number) in the BLD to BC-N (25%) in LD (**Figure 7a**), suggesting different BCc formation pathways. Despite the abrupt reductions of NO_x (-39%) due to the city lockdown, it is important to note that the concentration of $PM_{2.5}$ only slightly decreased during LD (-1%), highlighting the non-linear relationship between primary emissions and $PM_{2.5}$ levels.

During ALD ($PM_{2.5}$: 26.7 μg m^{-3}, NO_x: 27.9 μg m^{-3}, TVOC: 76.0 μg m^{-3}), the number fraction of BC-fresh particles rose from 28% (LD) to 31% (ALD), while the fraction of VE particles also increased from 3% (LD) to 12% (ALD) (**Figure 7a)**. Notably, the size distributions of BC-fresh and BC-aged particles presented relatively small peaks at 690

nm and 820 nm during ALD, in addition to the prominent peaks at 490 nm and 500 nm, which were different from those in the BLD and LD periods. These small peaks were relatively close to the dominant sizes of BC-fresh and BC-aged particles during LD (**Figure 6**). This result suggests that a substantial number of BCc with small sizes (around 500 nm) after the lockdown was lifted in Yangzhou, owing to the sudden enhancement of primary emissions; on the other hand, particles with large diameters (>690 nm) may have formed due to the participation of more trace reactive gases (e.g., NO_x, SO_2, and VOCs) in continuous aging reactions, resulting in thicker coatings on the surface of pre-existing particles and therefore a more clear separation of two-mode sizes during the ALD period than during the other two periods. This hypothesis was also supported by the increased number fraction of BCOC-SN during the ALD period (**Figure 7a**). Similar findings have been reported in the North China Plain (NCP) and the YRD during cold seasons, where thicker coatings on secondary aerosols were also observed under lower RH (<70%) (Zhang et al., 2021). This might be due to that particles with more organics and nitrate can result in earlier deliquescence and provide aqueous surfaces that facilitate the heterogeneous formation of secondary species under relatively low RH (Zhang et al., 2021). Among the three periods, the difference between the mode sizes of BC-aged and BC-fresh particles was the smallest (10 nm) during the ALD period (**Figure 6a and b**). This size reduction can be attributed to the increased BCOC and hydrophobic primary particles after lockdown (Figure 7). Because the internally mixed BCOC and hydrophobic primary particles may constrain further growth of secondary BC-SNA particles (Liu et al., 2016; Zhang et al., 2018), thereby leading to smaller-sized BC-aged particles. Moreover, the differences in BCc mode sizes between ALD and BLD periods also reveal an interesting fact that the lockdown effect may not only affect air quality during lockdown but also can influence the air quality even after lockdown, as the resumed emissions after lockdown may be subjected to different chemistry from that before lockdown.

Throughout the entire observation, the changes in the number fraction of BC-SNA exhibited consistency with the variations in RH (**Figure 7b**), indicating that BC tends to mix with ammonium sulfate and ammonium nitrate under high RH conditions. Meanwhile, the number fraction of BCOC shows similar patterns as TVOC, suggesting that high TVOC levels may facilitate the coating of organics on BC cores under low RH condition. **Figure 8** displays the number fraction of BCc species as a function of $PM_{2.5}$. Overall, as $PM_{2.5}$ levels increased, the number fraction of BC-aged particles also increased, while the proportion of BC-fresh particles decreased during BLD and LD, indicating a clear transition from BC-fresh particles to more aged ones, in line with the average size distribution during ALD has a small peak at 900 nm. Specifically, the increase in $PM_{2.5}$ was driven by BCOC-S during BLD (**Figure 8a**), whereas BC-N played a vital role in the $PM_{2.5}$ increase during LD (**Figure 8b**). Interestingly, the concentration of NO_x, the primary precursor of BC-N, decreased by 31% and 41% during LD compared to BLD and ALD, respectively (**Figure 3)**, indicating a strong

non-linear response of nitrate in BCc to NO_x, likely due to much faster conversion of NO_x to nitrate upon enhanced atmospheric oxidation capacity; additionally, the high proportion of BC-N during LD might be attributed to regional transport, similar to that in Shanghai during 2020 winter lockdown (Chang et al., 2020).

3.3 Chemical aging of BCc

As shown in **Figure 5**, in the average positive mass spectra of total BCc, the peak areas of C_n^+, OM, and metals contributed to more than 95% of the total, while nitrate and sulfate peak areas accounted for more than 90% of the negative mass spectral signal. To better elucidate the aging processes of BCc during different lockdown periods, we summed the carbon clusters $C_n^{\pm}$ (n = 1~5, accounting for more than 99% of C_n) peak areas to represent BC, and the total peak area of sulfate, nitrate, and ammonium (SNA) to represent the second inorganic components coated on BC. Additionally, we defined the sum of positive peak areas, excluding C_n^+ and metals, as OC to represent the OM coated on BC. These peak areas encompassed almost all the coating materials, except for metals, of BCc. The changes in the mixing state and morphology of BCc can provide insights into their aging characteristics, as reported previously (Kandler et al., 2018; Moffet et al., 2013). In this study, we use OC/C_n and SNA/C_n ratios to describe different types of chemical components coated on BC-fresh, and we use the ratio of the mode size of BC-aged (D_{aged}) to that of contemporaneous BC-fresh (D_{fresh}) to represent the aging degree of BCc.

Figure 9 illustrates the diurnal variations of the OC/C_n and SNA/C_n ratios along with the size distribution of BCc during different periods. We observed that both OC/C_n and SNA/C_n increased during nighttime and decreased during daytime. These variations showed the prominent enhancements of nocturnal OM and SNA, which could be attributed to the accelerated gas-to-particle partitioning and nocturnal secondary formation of organic/inorganic components under high relative humidity (RH > 85%) and relatively stagnant air mass (WS < 3 m s^{-1}) (**Figure S5**). It is worth noting that from BLD to LD and ALD, the intensity of diurnal variations of OC/C_n and SNA/C_n increased obviously. This discrepancy can be attributed to several reasons. (i) During BLD, the frequent precipitations effectively scavenged the particles (Isokääntä et al., 2022); (ii) In contrast, stronger solar radiation and higher O_3 concentration during LD promoted photochemical formations of OC and SNA; (iii) After lockdown, more precursors due to increased local emissions may lead to more production of secondary components than that during BLD as explained earlier. These results indicate that the aging process and mixing state of BCc depend strongly on meteorological conditions as well as emission sources in urban cities.

As shown in **Figure 9**, BCc with ~400 nm D_{va} exhibited significant diurnal fluctuations in the OC/C_n and SNA/C_n ratios, during LD. There is a noticeable increase in the proportion of BC-SNA particles during nighttime when RH is relatively high. These

observations suggest that nighttime heterogeneous hydrolysis may be considered a key mechanism responsible for the formation of BCOC and BC-SNA particles. According to Jacobson (2002), coagulation can be significant between particles with sizes <100nm and >1μm but insignificant for particles of >300nm, when the total particle number concentration is higher than 10^4 cm^{-3}. During LD, the OC/C_n and SNA/C_n ratios of BCc with ~400 nm D_{va} exhibited pronounced diurnal variations (**Figure 9**) and the number fraction of BC-SNA increased obviously. Despite the difference between D_{va} and physical diameter, such results imply that chemical reactions should be considered as the major pathway for BCOC and BC-SNA particles of ~400 nm D_{va}, while the large-sized BC-aged particles (>1 μm) may be partially from physical coagulation. Additionally, the larger mode peak (600 nm, D_{va}) and higher D_{aged}/D_{fresh} ratios (1.11) were observed compared to those of BLD (510 nm, 1.03) and ALD (500 nm, 1.02) (**Figure 6**). Since RH was significantly higher during LD (average RH of 87%) than BLD (average RH of 81%) and ALD period (average RH of 75%), this result again supports that aqueous or heterogeneous reactions might play a more important role to facilitate the chemical conversion of trace reactive gases (e.g., SO_2, NO_x, and VOCs) and then formed a thicker coating on the surfaces of BC cores, leading to evident growth in the size of BCc. This aqueous or heterogeneous process during LD likely converted partially coated particles to fully thickly coated BCc as well.

3.4 Source apportionment of BCc during lockdown

In addition to local emissions, regional transport plays a significant role in influencing pollutant levels. The emergent lockdown in Yangzhou led to strict limitation on local emissions, while surrounding cities were still running as usual. This is supported by **Figure S6**, which illustrates the $PM_{2.5}$ concentrations in Yangzhou and the other five surrounding YRD cities (e.g., Nanjing, Zhenjiang, Changzhou, Taizhou, and Chuzhou) during the campaign. High correlations between $PM_{2.5}$ concentrations in Yangzhou and the other five cities were observed across all different periods (**Figure S6**). These findings underscore the importance of the regional transport in $PM_{2.5}$ pollution during the campaign, providing a unique opportunity to investigate the transmission and source characteristics of BCc in YRD during summer. Herein, PSCF analysis was applied to qualitatively simulate the source probability distributions of the specific BCc particle types (BC-fresh, BC-aged, BCOC, and BC-SNA) during LD.

As shown in **Figure 10**, the hotspots of potential sources for the four particle types exhibited strong agreements with each other and primarily concentrated in the southeast of Yangzhou, especially along the coast of the Yangtze River, with the WPSCF greater than 0.6. These hotspot areas also encompassed chemical enterprises, power plants, petrochemical industrial parks, and the Yangtze River in the YRD. This evidence suggests that the region of southeast Yangzhou and lower reaches of the Yangtze River are major source areas for the regionally transported BCc in Yangzhou during lockdown. Additionally, Luo et al. (2023) reported that regional transport of pollutants can occur

near the surface from upwind areas when the wind speed (WS) exceeds 2 m s^{-1}. **Figure S5b** shows that the mean daytime WS was 3 m s^{-1}, indicating that both BC-fresh and BC-aged particles, along with trace gases (e.g., SO_2, NO_x, and VOCs), originating from the hotspot areas, could be transported effectively to Yangzhou. Additionally, the average size of BCc remained around 600 nm at daytime (**Figure S5c**), suggesting that BCc could undergo continual aging reactions under relatively lower RH, but produce relatively thinly coated BCc with smaller sizes than those at nighttime (average size of 650 nm). The mean nocturnal WS decreased to 2 m s^{-1}, indicating that the regional atmosphere becomes stagnant (**Figures S5a, b)**. As mentioned earlier and underscored here again, this stagnant and humid atmospheric condition may promote aqueous or heterogeneous reactions, likely further leading to the production of more thickly coated BCc than daytime ones.

4. Conclusions and implications

During the summer of 2021, the COVID-19 lockdown imposed in Yangzhou resulted in a significant decrease in anthropogenic emissions from traffic and manufacturing sectors. To examine the effects of this lockdown, we utilized spaceborne observations, ground-based measurements, and particularly SPA-MS analysis to explore the variations, aging characteristics, and sources of BCc in the YRD. We showed that the strict emission controls effectively reduced local gaseous pollutants. However, the decline in NO_x (-39%) and TVOC (-14%) levels might on the other hand result in increased O_3 (28%), leading to a rise in BC-aged particles and a slight elevation in $PM_{2.5}$ levels during the lockdown. Our results revealed a strong non-linear response of $PM_{2.5}$ and O_3 to the gaseous precursors.

The SPA-MS analysis results further demonstrate significant enhancement of OM and SNA coating species on BC-fresh particles, owing to gas-to-particle partitioning and nocturnal multiphase chemistry. Consequently, we observed a higher fraction of BC-aged particles (73%) during the lockdown due to enhanced oxidizing capacity and high relative humidity (RH > 85%). The BC-fresh particles tended to mix with SNA under high RH conditions, while high TVOC levels were accompanied by BCOC formation. However, BCOC particles generally exhibited smaller sizes compared to BC-SNA particles. Moreover, we propose that aqueous or heterogeneous reactions might be important to generate BCOC and BC-SNA particles, especially ones with 400 nm D_{va}, while coagulation might play a more prominent role in larger BC-aged particles. The aging process during LD promoted the conversion of partly coated particles to totally coated ones, with larger diameters (600 nm) and thicker coatings.

It should be noted that the observed average $PM_{2.5}$ concentration during the lockdown in Yangzhou was 20 μg m^{-3}, which still significantly exceeds the WHO's air quality guideline of 5 μg m^{-3}. Our research underscores the crucial role of BCc, which constitutes a significant portion of $PM_{2.5}$, in particulate matter pollution. These particles

originate from diverse combustion sources and their behavior is intricately influenced by complex chemistry, regional transport, and meteorological factors. Mere reductions in local primary emissions from traffic and manufacturing sectors exhibit limited efficacy in air quality improvement. Therefore, effective air quality remediation strategies necessitate nuanced control of BCc alongside broader emission reduction efforts. We suggest a more comprehensive regulation of precursor gases from multiple sectors, a wide-ranging joint regulation approach as well as proper consideration of the chemistry, to develop an effective strategy for air quality improvement.

Data availability. The data in this study are available from the corresponding author upon request (caxinra@163.com).

Author contributions. XG, JW, and YD designed the research. YD, HW, and SC conducted the field measurements. YD, HW, JW, and SC analyzed the data. XG, JW, HL, YW, YZ, and EA reviewed the paper and provided useful suggestions. YD, JW, and XG wrote the first draft of the paper. All people were involved in the discussion of the results.

Supplement. The supplement related to this article is available online at XXX.

Competing interests. The contact author has declared that neither they nor their co-authors have any competing interests.

Financial support. This research has been supported by the National Natural Science Foundation of China (grant nos. 42377100, 22276099, and 42021004).

References

Adachi, K., Zaizen, Y., Kajino, M., Igarashi, Y., 2014. Mixing state of regionally transported soot particles and the coating effect on their size and shape at a mountain site in Japan. Journal of Geophysical Research: Atmospheres 119, 5386–5396. https://doi.org/10.1002/2013JD020880

Benedetti, A., Morcrette, J.-J., Boucher, O., Dethof, A., Engelen, R.J., Fisher, M., Flentje, H., Huneeus, N., Jones, L., Kaiser, J.W., Kinne, S., Mangold, A., Razinger, M., Simmons, A.J., Suttie, M., 2009. Aerosol analysis and forecast in the European Centre for Medium-Range Weather Forecasts Integrated Forecast System: 2. Data assimilation. Journal of Geophysical Research: Atmospheres 114. https://doi.org/10.1029/2008JD011115

Bond, T.C., Bergstrom, R.W., 2006. Light Absorption by Carbonaceous Particles: An Investigative Review. Aerosol Science and Technology 40, 27–67. https://doi.org/10.1080/02786820500421521

Bond, T.C., Doherty, S., Fahey, D.W., Forster, P., Berntsen, T., DeAngelo, B., Flanner, M., Ghan, S., Kärcher, B., Koch, D., Kinne, S., Kondo, Y., Quinn, P.K., Sarofim, M., Schultz, M., Michael, S., Venkataraman, C., Zhang, H., Zhang, S., Zender, C.S., 2013. Bounding the role of black carbon in the climate system: A Scientific assessment. Journal of Geophysical Research: Atmospheres 118, 5380–5552. https://doi.org/10.1002/jgrd.50171

Cappa, C.D., Zhang, X., Russell, L.M., Collier, S., Lee, A.K.Y., Chen, C.-L., Betha, R., Chen, S., Liu, J., Price, D.J., Sanchez, K.J., McMeeking, G.R., Williams, L.R., Onasch, T.B., Worsnop, D.R., Abbatt, J., Zhang, Q., 2019. Light Absorption by Ambient Black and Brown Carbon and its Dependence on Black Carbon Coating State for Two California, USA, Cities in Winter and Summer. Journal of Geophysical Research: Atmospheres 124, 1550–1577. https://doi.org/10.1029/2018JD029501

Chang, Y., Huang, R., Ge, X., Huang, X., Hu, J., Duan, Y., Zou, Z., Liu, X., Lehmann, M.F., 2020. Puzzling Haze Events in China During the Coronavirus (COVID-19) Shutdown. Geophys. Res. Lett. 47. https://doi.org/10.1029/2020GL088533

Chen, H., Huo, J., Fu, Q., Duan, Y., Xiao, H., Chen, J., 2020. Impact of quarantine measures on chemical compositions of PM2.5 during the COVID-19 epidemic in Shanghai, China. Science of The Total Environment 743, 140758. https://doi.org/10.1016/j.scitotenv.2020.140758

Chen, L., Qi, X., Nie, W., Wang, J., Xu, Zheng, Wang, T., Liu, Y., Shen, Y., Xu, Zhengning, Kokkonen, T., Chi, X., Aalto, P., Paasonen, P., Kerminen, V.-M., Petäjä, T., Kulmala, M., Ding, A., 2021. Cluster Analysis of Submicron Particle Number Size Distributions at the SORPES Station in the Yangtze River Delta of East China. Journal of Geophysical Research: Atmospheres 126. https://doi.org/10.1029/2020JD034004

Chen, L., Zhang, F., Yan, P., Wang, X., Sun, L., Li, Y., Zhang, X., Sun, Y., Li, Z., 2020. The large proportion of black carbon (BC)-containing aerosols in the urban

atmosphere. Environmental Pollution 263, 114507. https://doi.org/10.1016/j.envpol.2020.114507

Cheng, Y.F., Su, H., Rose, D., Gunthe, S.S., Berghof, M., Wehner, B., Achtert, P., Nowak, A., Takegawa, N., Kondo, Y., Shiraiwa, M., Gong, Y.G., Shao, M., Hu, M., Zhu, T., Zhang, Y.H., Carmichael, G.R., Wiedensohler, A., Andreae, M.O., Pöschl, U., 2012. Size-resolved measurement of the mixing state of soot in the megacity Beijing, China: diurnal cycle, aging and parameterization. Atmospheric Chemistry and Physics 12, 4477–4491. https://doi.org/10.5194/acp-12-4477-2012

Chien, L.-C., Chen, L.-W.A., Lin, R.-T., 2022. Lagged meteorological impacts on COVID-19 incidence among high-risk counties in the United States—a spatiotemporal analysis. J Expo Sci Environ Epidemiol 32, 774–781. https://doi.org/10.1038/s41370-021-00356-y

Clemente, Á., Yubero, E., Nicolás, J.F., Caballero, S., Crespo, J., Galindo, N., 2022. Changes in the concentration and composition of urban aerosols during the COVID-19 lockdown. Environmental Research 203, 111788. https://doi.org/10.1016/j.envres.2021.111788

Cui, S., Xian, J., Shen, F., Zhang, L., Deng, B., Zhang, Y., Ge, X., 2021. One-Year Real-Time Measurement of Black Carbon in the Rural Area of Qingdao, Northeastern China: Seasonal Variations, Meteorological Effects, and the COVID-19 Case Analysis. Atmosphere 12, 394. https://doi.org/10.3390/atmos12030394

Cui, Y., Ji, D., Maenhaut, W., Gao, W., Zhang, R., Wang, Y., 2020. Levels and sources of hourly PM2.5-related elements during the control period of the COVID-19 pandemic at a rural site between Beijing and Tianjin. Science of The Total Environment 744, 140840. https://doi.org/10.1016/j.scitotenv.2020.140840

Ding, A., Huang, X., Nie, W., Chi, X., Xu, Zheng, Zheng, L., Xu, Zhengning, Xie, Y., Qi, X., Shen, Y., Sun, P., Wang, J., Wang, L., Sun, J., Yang, X.-Q., Qin, W., Zhang, X., Cheng, W., Liu, W., Pan, L., Fu, C., 2019. Significant reduction of $PM_{2.5}$ in eastern China due to regional-scale emission control: evidence from SORPES in 2011–2018. Atmospheric Chemistry and Physics 19, 11791–11801. https://doi.org/10.5194/acp-19-11791-2019

Ding, S., Liu, D., Hu, K., Zhao, D., Tian, P., Wang, F., Li, R., Chen, Y., He, H., Huang, M., Ding, D., 2021. Optical and hygroscopic properties of black carbon influenced by particle microphysics at the top of the anthropogenically polluted boundary layer. Atmospheric Chemistry & Physics 21, 681–694. https://doi.org/10.5194/acp-21-681-2021

Feng, Z., Zheng, F., Liu, Y., Fan, X., Yan, C., Zhang, Y., Daellenbach, K.R., Bianchi, F., Petäjä, T., Kulmala, M., Bao, X., 2022. Evolution of organic carbon during COVID-19 lockdown period: Possible contribution of nocturnal chemistry. Sci Total Environ 808, 152191. https://doi.org/10.1016/j.scitotenv.2021.152191

Ge, B., Xu, D., Wild, O., Yao, X., Wang, J., Chen, X., Qixin, T., Pan, X., Wang, Z., 2020. Inter-annual variations of wet deposition in Beijing during 2014–2017:

649 implications of below-cloud scavenging of inorganic aerosols.
650 https://doi.org/10.5194/acp-2020-1146
651 Gorelick, N., Hancher, M., Dixon, M., Ilyushchenko, S., Thau, D., Moore, R., 2017.
652 Google Earth Engine: Planetary-scale geospatial analysis for everyone. Remote
653 Sensing of Environment, Big Remotely Sensed Data: tools, applications and
654 experiences 202, 18–27. https://doi.org/10.1016/j.rse.2017.06.031
655 He, C., Liou, K.-N., Takano, Y., Zhang, R., Levy Zamora, M., Yang, P., Li, Q., Leung,
656 L.R., 2015. Variation of the radiative properties during black carbon aging:
657 theoretical and experimental intercomparison. Atmospheric Chemistry and
658 Physics 15, 11967–11980. https://doi.org/10.5194/acp-15-11967-2015
659 Hopke, P.K., Gao, N., Cheng, M.-D., 1993. Combining chemical and meteorological
660 data to infer source areas of airborne pollutants. Chemometrics and Intelligent
661 Laboratory Systems, Proceedings of the 5th Conference on Computer
662 Applications in Analytical Chemistry (COMPANA '92) 19, 187–199.
663 https://doi.org/10.1016/0169-7439(93)80103-O
664 Huang, X., Ding, A., Gao, J., Zheng, B., Zhou, D., Qi, X., Tang, R., Wang, J., Ren, C.,
665 Nie, W., Chi, X., Xu, Z., Chen, L., Li, Y., Che, F., Pang, N., Wang, H., Tong, D.,
666 Qin, W., Cheng, W., Liu, W., Fu, Q., Liu, B., Chai, F., Davis, S.J., Zhang, Q.,
667 He, K., 2021. Enhanced secondary pollution offset reduction of primary
668 emissions during COVID-19 lockdown in China. Natl Sci Rev 8, nwaa137.
669 https://doi.org/10.1093/nsr/nwaa137
670 Huang, X., Wang, Z., Ding, A., 2018. Impact of Aerosol-PBL Interaction on Haze
671 Pollution: Multiyear Observational Evidences in North China. Geophysical
672 Research Letters 45, 8596–8603. https://doi.org/10.1029/2018GL079239
673 Isokääntä, S., Kim, P., Mikkonen, S., Kühn, T., Kokkola, H., Yli-Juuti, T., Heikkinen,
674 L., Luoma, K., Petäjä, T., Kipling, Z., Partridge, D., Virtanen, A., 2022. The
675 effect of clouds and precipitation on the aerosol concentrations and composition
676 in a boreal forest environment. Atmospheric Chemistry and Physics 22, 11823–
677 11843. https://doi.org/10.5194/acp-22-11823-2022
678 Jacobson, M.Z., 2002. Analysis of aerosol interactions with numerical techniques for
679 solving coagulation, nucleation, condensation, dissolution, and reversible
680 chemistry among multiple size distributions. Journal of Geophysical Research:
681 Atmospheres 107, AAC 2-1-AAC 2-23. https://doi.org/10.1029/2001JD002044
682 Jain, C.D., Madhavan, B.L., Singh, V., Prasad, P., Sai Krishnaveni, A., Ravi Kiran, V.,
683 Venkat Ratnam, M., 2021. Phase-wise analysis of the COVID-19 lockdown
684 impact on aerosol, radiation and trace gases and associated chemistry in a
685 tropical rural environment. Environmental Research 194, 110665.
686 https://doi.org/10.1016/j.envres.2020.110665
687 Jeong, C.-H., Yousif, M., Evans, G.J., 2022. Impact of the COVID-19 lockdown on the
688 chemical composition and sources of urban PM2.5. Environmental Pollution
689 292, 118417. https://doi.org/10.1016/j.envpol.2021.118417
690 Kahnert, M., 2010. On the Discrepancy between Modeled and Measured Mass

691 Absorption Cross Sections of Light Absorbing Carbon Aerosols. Aerosol
692 Science and Technology 44, 453–460.
693 https://doi.org/10.1080/02786821003733834
694 Kandler, K., Schneiders, K., Ebert, M., Hartmann, M., Weinbruch, S., Prass, M.,
695 Pöhlker, C., 2018. Composition and mixing state of atmospheric aerosols
696 determined by electron microscopy: method development and application to
697 aged Saharan dust deposition in the Caribbean boundary layer. Atmospheric
698 Chemistry and Physics 18, 13429–13455. https://doi.org/10.5194/acp-18-
699 13429-2018
700 Kondo, Y., Matsui, H., Moteki, N., Sahu, L., Takegawa, N., Kajino, M., Zhao, Y.,
701 Cubison, M.J., Jimenez, J.L., Vay, S., Diskin, G.S., Anderson, B., Wisthaler, A.,
702 Mikoviny, T., Fuelberg, H.E., Blake, D.R., Huey, G., Weinheimer, A.J., Knapp,
703 D.J., Brune, W.H., 2011. Emissions of black carbon, organic, and inorganic
704 aerosols from biomass burning in North America and Asia in 2008. Journal of
705 Geophysical Research: Atmospheres 116.
706 https://doi.org/10.1029/2010JD015152
707 Laughner, J.L., Neu, J.L., Schimel, D., Wennberg, P.O., Barsanti, K., Bowman, K.W.,
708 Chatterjee, A., Croes, B.E., Fitzmaurice, H.L., Henze, D.K., Kim, J., Kort, E.A.,
709 Liu, Z., Miyazaki, K., Turner, A.J., Anenberg, S., Avise, J., Cao, H., Crisp, D.,
710 de Gouw, J., Eldering, A., Fyfe, J.C., Goldberg, D.L., Gurney, K.R.,
711 Hasheminassab, S., Hopkins, F., Ivey, C.E., Jones, D.B.A., Liu, J., Lovenduski,
712 N.S., Martin, R.V., McKinley, G.A., Ott, L., Poulter, B., Ru, M., Sander, S.P.,
713 Swart, N., Yung, Y.L., Zeng, Z.-C., 2021. Societal shifts due to COVID-19
714 reveal large-scale complexities and feedbacks between atmospheric chemistry
715 and climate change. Proc Natl Acad Sci U S A 118, e2109481118.
716 https://doi.org/10.1073/pnas.2109481118
717 Le, T., Wang, Y., Liu, L., Yang, J., Yung, Y.L., Li, G., Seinfeld, J.H., 2020. Unexpected
718 air pollution with marked emission reductions during the COVID-19 outbreak
719 in China. Science 369, 702–706. https://doi.org/10.1126/science.abb7431
720 Li, J., Jiang, L., Chen, C., Liu, D., Du, S., Zhang, Y., Yang, Y., Tang, L., 2020.
721 Characteristics and Sources of Black Carbon Aerosol in a Mega-City in the
722 Western Yangtze River Delta, China. Atmosphere 11, 315.
723 https://doi.org/10.3390/atmos11040315
724 Li, K., Wang, X., Lu, X., Chen, H., Yang, X., 2022. Effects of Volatile Components on
725 Mixing State and Size Distribution of Individual Black Carbon Aerosols.
726 Aerosol Air Qual. Res. 22, 210400. https://doi.org/10.4209/aaqr.210400
727 Li, L., Huang, Z., Dong, J., Li, M., Gao, W., Nian, H., Fu, Z., Zhang, G., Bi, X., Cheng,
728 P., Zhou, Z., 2011. Real time bipolar time-of-flight mass spectrometer for
729 analyzing single aerosol particles. International Journal of Mass Spectrometry
730 303, 118–124. https://doi.org/10.1016/j.ijms.2011.01.017
731 Li, L., Li, Q., Huang, L., Wang, Q., Zhu, A., Xu, J., Liu, Ziyi, Li, H., Shi, L., Li, R.,
732 Azari, M., Wang, Y., Zhang, X., Liu, Zhiqiang, Zhu, Y., Zhang, K., Xue, S., Ooi,

M.C.G., Zhang, D., Chan, A., 2020. Air quality changes during the COVID-19 lockdown over the Yangtze River Delta Region: An insight into the impact of human activity pattern changes on air pollution variation. Science of The Total Environment 732, 139282. https://doi.org/10.1016/j.scitotenv.2020.139282

Liu, D., Joshi, R., Wang, J., Yu, C., Allan, J.D., Coe, H., Flynn, M.J., Xie, C., Lee, J., Squires, F., Kotthaus, S., Grimmond, S., Ge, X., Sun, Y., Fu, P., 2019. Contrasting physical properties of black carbon in urban Beijing between winter and summer. Atmospheric Chemistry and Physics 19, 6749–6769. https://doi.org/10.5194/acp-19-6749-2019

Liu, Q., Jing, B., Peng, C., Tong, S., Wang, W., Ge, M., 2016. Hygroscopicity of internally mixed multi-component aerosol particles of atmospheric relevance. Atmospheric Environment 125, 69–77. https://doi.org/10.1016/j.atmosenv.2015.11.003

Luo, J., Li, Z., Zhang, C., Zhang, Q., Zhang, Yongming, Zhang, Ying, Curci, G., Chakrabarty, R.K., 2022. Regional impacts of black carbon morphologies on shortwave aerosol–radiation interactions: a comparative study between the US and China. Atmospheric Chemistry and Physics 22, 7647–7666. https://doi.org/10.5194/acp-22-7647-2022

Moffet, R.C., Rödel, T.C., Kelly, S.T., Yu, X.Y., Carroll, G.T., Fast, J., Zaveri, R.A., Laskin, A., Gilles, M.K., 2013. Spectro-microscopic measurements of carbonaceous aerosol aging in Central California. Atmospheric Chemistry and Physics 13, 10445–10459. https://doi.org/10.5194/acp-13-10445-2013

Morcrette, J.-J., Boucher, O., Jones, L., Salmond, D., Bechtold, P., Beljaars, A., Benedetti, A., Bonet, A., Kaiser, J.W., Razinger, M., Schulz, M., Serrar, S., Simmons, A.J., Sofiev, M., Suttie, M., Tompkins, A.M., Untch, A., 2009. Aerosol analysis and forecast in the European Centre for Medium-Range Weather Forecasts Integrated Forecast System: Forward modeling. Journal of Geophysical Research: Atmospheres 114. https://doi.org/10.1029/2008JD011235

Nie, D., Shen, F., Wang, J., Ma, X., Li, Z., Ge, P., Ou, Y., Jiang, Y., Chen, Meijuan, Chen, Mindong, Wang, T., Ge, X., 2021. Changes of air quality and its associated health and economic burden in 31 provincial capital cities in China during COVID-19 pandemic. Atmos Res 249, 105328. https://doi.org/10.1016/j.atmosres.2020.105328

Peng, J., Hu, M., Guo, S., Du, Z., Zheng, Jing, Shang, D., Levy Zamora, M., Zeng, L., Shao, M., Wu, Y.-S., Zheng, Jun, Wang, Y., Glen, C.R., Collins, D.R., Molina, M.J., Zhang, R., 2016. Markedly enhanced absorption and direct radiative forcing of black carbon under polluted urban environments. Proceedings of the National Academy of Sciences 113, 4266–4271. https://doi.org/10.1073/pnas.1602310113

Polissar, A.V., Hopke, P.K., Paatero, P., Kaufmann, Y.J., Hall, D.K., Bodhaine, B.A., Dutton, E.G., Harris, J.M., 1999. The aerosol at Barrow, Alaska: long-term

trends and source locations. Atmospheric Environment 33, 2441–2458. https://doi.org/10.1016/S1352-2310(98)00423-3
Qin, M., Hu, A., Mao, J., Li, X., Sheng, L., Sun, J., Li, J., Wang, X., Zhang, Y., Hu, J., 2021. PM2.5 and O3 relationships affected by the atmospheric oxidizing capacity in the Yangtze River Delta, China. Science of The Total Environment 152268. https://doi.org/10.1016/j.scitotenv.2021.152268
Ramanathan, V., Carmichael, G., 2008. Global and regional climate changes due to black carbon. Nature Geoscience 1, 221–227. https://doi.org/10.1038/ngeo156
Sedlacek, A.J., Lewis, E.R., Onasch, T.B., Zuidema, P., Redemann, J., Jaffe, D., Kleinman, L.I., 2022. Using the Black Carbon Particle Mixing State to Characterize the Lifecycle of Biomass Burning Aerosols. Environ. Sci. Technol. 56, 14315–14325. https://doi.org/10.1021/acs.est.2c03851
Silva, P.J., Liu, D.-Y., Noble, C.A., Prather, K.A., 1999. Size and Chemical Characterization of Individual Particles Resulting from Biomass Burning of Local Southern California Species. Environ. Sci. Technol. 33, 3068–3076. https://doi.org/10.1021/es980544p
Song, X.-H., Hopke, P.K., Fergenson, D.P., Prather, K.A., 1999. Classification of Single Particles Analyzed by ATOFMS Using an Artificial Neural Network, ART-2A. Anal. Chem. 71, 860–865. https://doi.org/10.1021/ac9809682
Steinfeld, J.I., 1998. Atmospheric Chemistry and Physics: From Air Pollution to Climate Change. Environment: Science and Policy for Sustainable Development 40, 26–26. https://doi.org/10.1080/00139157.1999.10544295
Sulaymon, I.D., Zhang, Yuanxun, Hopke, P.K., Hu, J., Zhang, Yang, Li, L., Mei, X., Gong, K., Shi, Z., Zhao, B., Zhao, F., 2021a. Persistent high PM2.5 pollution driven by unfavorable meteorological conditions during the COVID-19 lockdown period in the Beijing-Tianjin-Hebei region, China. Environmental Research 198, 111186. https://doi.org/10.1016/j.envres.2021.111186
Sulaymon, I.D., Zhang, Yuanxun, Hopke, P.K., Zhang, Yang, Hua, J., Mei, X., 2021b. COVID-19 pandemic in Wuhan: Ambient air quality and the relationships between criteria air pollutants and meteorological variables before, during, and after lockdown. Atmospheric Research 250, 105362. https://doi.org/10.1016/j.atmosres.2020.105362
Sun, J., Sun, Y., Xie, C., Xu, Weiqi, Chen, C., Wang, Zhe, Li, L., Du, X., Huang, F., Li, Y., Li, Z., Pan, X., Ma, N., Xu, Wanyun, Fu, P., Wang, Zifa, 2022. The chemical composition and mixing state of BC-containing particles and the implications on light absorption enhancement. Atmos. Chem. Phys. 22, 7619–7630. https://doi.org/10.5194/acp-22-7619-2022
Sun, J., Wang, Zhe, Zhou, W., Xie, C., Wu, C., Chen, C., Han, T., Wang, Q., Li, Z., Li, J., Fu, P., Wang, Zifa, Sun, Y., 2021. Measurement report: Long-term changes in black carbon and aerosol optical properties from 2012 to 2020 in Beijing, China (preprint). Aerosols/Field Measurements/Troposphere/Physics (physical properties and processes). https://doi.org/10.5194/acp-2021-637

817 Sun, Y., Du, W., Fu, P., Wang, Q., Li, J., Ge, X., Zhang, Q., Zhu, C., Ren, L., Xu, W.,
818 Zhao, J., Han, T., Worsnop, D.R., Wang, Z., 2016. Primary and secondary
819 aerosols in Beijing in winter: sources, variations and processes. Atmos. Chem.
820 Phys.
821 Sun, Y., Lei, L., Zhou, W., Chen, C., He, Y., Sun, J., Li, Z., Xu, W., Wang, Q., Ji, D., Fu,
822 P., Wang, Z., Worsnop, D.R., 2020. A chemical cocktail during the COVID-19
823 outbreak in Beijing, China: Insights from six-year aerosol particle composition
824 measurements during the Chinese New Year holiday. Science of The Total
825 Environment 742, 140739. https://doi.org/10.1016/j.scitotenv.2020.140739
826 Taylor, J.W., Allan, J.D., Allen, G., Coe, H., Williams, P.I., Flynn, M.J., Le Breton, M.,
827 Muller, J.B.A., Percival, C.J., Oram, D., Forster, G., Lee, J.D., Rickard, A.R.,
828 Parrington, M., Palmer, P.I., 2014. Size-dependent wet removal of black carbon
829 in Canadian biomass burning plumes. Atmospheric Chemistry and Physics 14,
830 13755–13771. https://doi.org/10.5194/acp-14-13755-2014
831 Wang, H., Miao, Q., Shen, L., Yang, Q., Wu, Y., Wei, H., 2021. Air pollutant variations
832 in Suzhou during the 2019 novel coronavirus (COVID-19) lockdown of 2020:
833 High time-resolution measurements of aerosol chemical compositions and
834 source apportionment. Environmental Pollution 271, 116298.
835 https://doi.org/10.1016/j.envpol.2020.116298
836 Wang, J., Ge, X., Sonya, C., Ye, J., Lei, Y., Chen, M., Zhang, Q., 2022. Influence of
837 regional emission controls on the chemical composition, sources, and size
838 distributions of submicron aerosols: Insights from the 2014 Nanjing Youth
839 Olympic Games. Science of The Total Environment 807, 150869.
840 https://doi.org/10.1016/j.scitotenv.2021.150869
841 Wang, J., Liu, D., Ge, X., Wu, Y., Shen, F., Chen, M., Zhao, J., Xie, C., Wang, Q., Xu,
842 W., Zhang, J., Hu, J., Allan, J., Joshi, R., Fu, P., Coe, H., Sun, Y., 2019.
843 Characterization of black carbon-containing fine particles in Beijing during
844 wintertime. Atmos. Chem. Phys. 19, 447–458. https://doi.org/10.5194/acp-19-
845 447-2019
846 Wang, Pengfei, Chen, K., Zhu, S., Wang, Peng, Zhang, H., 2020. Severe air pollution
847 events not avoided by reduced anthropogenic activities during COVID-19
848 outbreak. Resources, Conservation and Recycling 158, 104814.
849 https://doi.org/10.1016/j.resconrec.2020.104814
850 Wang, Q., Liu, S., Zhou, Y., Cao, J., Han, Y., Ni, H., Zhang, N., Huang, R., 2015.
851 Characteristics of Black Carbon Aerosol during the Chinese Lunar Year and
852 Weekdays in Xi'an, China. Atmosphere 6, 195–208.
853 https://doi.org/10.3390/atmos6020195
854 Wang, S., Zhao, M., Xing, J., Wu, Y., Zhou, Y., Lei, Y., He, K., Fu, L., Hao, J., 2010.
855 Quantifying the Air Pollutants Emission Reduction during the 2008 Olympic
856 Games in Beijing. Environ. Sci. Technol. 44, 2490–2496.
857 https://doi.org/10.1021/es9028167
858 Wang, Y., Zhu, S., Ma, J., Shen, J., Wang, Pengfei, Wang, Peng, Zhang, H., 2021.

Enhanced atmospheric oxidation capacity and associated ozone increases during COVID-19 lockdown in the Yangtze River Delta. Science of The Total Environment 768, 144796. https://doi.org/10.1016/j.scitotenv.2020.144796

Wang, Y.Q., 2014. MeteoInfo: GIS software for meteorological data visualization and analysis. Meteorological Applications 21, 360–368. https://doi.org/10.1002/met.1345

Wang, Y.Q., Zhang, X.Y., Draxler, R.R., 2009. TrajStat: GIS-based software that uses various trajectory statistical analysis methods to identify potential sources from long-term air pollution measurement data. Environmental Modelling & Software 24, 938–939. https://doi.org/10.1016/j.envsoft.2009.01.004

WHO global air quality guidelines: Particulate matter (PM2.5 and PM10), ozone, nitrogen dioxide, sulfur dioxide and carbon monoxide, 2021. , WHO Guidelines Approved by the Guidelines Review Committee. World Health Organization, Geneva.

Xie, C., He, Y., Lei, L., Zhou, W., Liu, J., Wang, Q., Xu, W., Qiu, Y., Zhao, J., Sun, J., Li, L., Li, M., Zhou, Z., Fu, P., Wang, Z., Sun, Y., 2020. Contrasting mixing state of black carbon-containing particles in summer and winter in Beijing. Environmental Pollution 263, 114455. https://doi.org/10.1016/j.envpol.2020.114455

Xu, J., Ge, X., Zhang, X., Zhao, W., Zhang, R., Zhang, Y., 2020. COVID-19 Impact on the Concentration and Composition of Submicron Particulate Matter in a Typical City of Northwest China. Geophysical Research Letters 47, e2020GL089035. https://doi.org/10.1029/2020GL089035

Yang, J., Ma, S., Gao, B., Li, X., Zhang, Y., Cai, J., Li, M., Yao, L., Huang, B., Zheng, M., 2017. Single particle mass spectral signatures from vehicle exhaust particles and the source apportionment of on-line PM2.5 by single particle aerosol mass spectrometry. Science of The Total Environment 593–594, 310–318. https://doi.org/10.1016/j.scitotenv.2017.03.099

Zhang, G., Fu, Y., Peng, X., Sun, W., Shi, Z., Song, W., Hu, W., Chen, D., Lian, X., Li, L., Tang, M., Wang, X., Bi, X., 2021. Black Carbon Involved Photochemistry Enhances the Formation of Sulfate in the Ambient Atmosphere: Evidence From In Situ Individual Particle Investigation. Geophys Res Atmos 126. https://doi.org/10.1029/2021JD035226

Zhang, J., Li, H., Chen, L., Huang, X., Zhang, W., Zhao, R., 2022. Particle composition, sources and evolution during the COVID-19 lockdown period in Chengdu, southwest China: Insights from single particle aerosol mass spectrometer data. Atmospheric Environment 268, 118844. https://doi.org/10.1016/j.atmosenv.2021.118844

Zhang, J., Yuan, Q., Liu, L., Wang, Y., Zhang, Y., Xu, L., Pang, Y., Zhu, Y., Niu, H., Shao, L., Yang, S., Liu, H., Pan, X., Shi, Z., Hu, M., Fu, P., Li, W., 2021. Trans-Regional Transport of Haze Particles From the North China Plain to Yangtze River Delta During Winter. JGR Atmospheres 126.

https://doi.org/10.1029/2020JD033778
Zhang, K., Liu, Z., Zhang, X., Li, Q., Jensen, A., Tan, W., Huang, L., Wang, Y., de Gouw, J., Li, L., 2022. Insights into the significant increase in ozone during COVID-19 in a typical urban city of China. Atmos. Chem. Phys. 22, 4853–4866. https://doi.org/10.5194/acp-22-4853-2022
Zhang, Y., Liu, X., Zhang, L., Tang, A., Goulding, K., Collett, J.L., 2021. Evolution of secondary inorganic aerosols amidst improving PM2.5 air quality in the North China plain. Environmental Pollution 281, 117027. https://doi.org/10.1016/j.envpol.2021.117027
Zhang Y., Wang X., Chen H., Yang X., Chen J., Alien J.O., 2009. Source Apportionment Of Lead-containing Aerosol Particles In Shanghai Using Single Particle Mass Spectrometry. Chemosphere 74, 501–507.
Zhang, Y., Yuan, Q., Huang, D., Kong, S., Zhang, J., Wang, X., Lu, C., Shi, Z., Zhang, X., Sun, Y., Wang, Z., Shao, L., Zhu, J., Li, W., 2018. Direct Observations of Fine Primary Particles From Residential Coal Burning: Insights Into Their Morphology, Composition, and Hygroscopicity. Journal of Geophysical Research: Atmospheres 123, 12,964-12,979. https://doi.org/10.1029/2018JD028988
Zhang, Z., Li, H., Ho, W., Cui, L., Men, Q., Cao, L., Zhang, Y., Wang, J., Huang, C., Lee, S., Huang, Y., Chen, M., Ge, X., 2024. Critical Roles of Surface-Enhanced Heterogeneous Oxidation of SO2 in Haze Chemistry: Review of Extended Pathways for Complex Air Pollution. Curr Pollution Rep. https://doi.org/10.1007/s40726-023-00287-2
Zhou, H., Liu, T., Sun, B., Tian, Y., Zhou, X., Hao, F., Chun, X., Wan, Z., Liu, P., Wang, J., Du, D., 2022. Chemical characteristics and sources of PM2.5 in Hohhot, a semi-arid city in northern China: insight from the COVID-19 lockdown. Atmos. Chem. Phys. 14.
Zhou, X., Gao, J., Wang, T., Wu, W., Wang, W., 2009. Measurement of black carbon aerosols near two Chinese megacities and the implications for improving emission inventories. Atmospheric Environment 43, 3918–3924. https://doi.org/10.1016/j.atmosenv.2009.04.062
Zhou, Y., Wu, Y., Yang, L., Fu, L., He, K., Wang, S., Hao, J., Chen, J., Li, C., 2010. The impact of transportation control measures on emission reductions during the 2008 Olympic Games in Beijing, China. Atmospheric Environment 44, 285–293. https://doi.org/10.1016/j.atmosenv.2009.10.040
Zhu, X., Hu, B., Xin, J., Wang, L., Münkel, C., Mao, G., Wang, Y., 2015. Impact of emission controls on air quality in Beijing during APEC 2014: Lidar ceilometer observations. ATMOSPHERIC CHEMISTRY AND PHYSICS 15, 12667–12680. https://doi.org/10.5194/acp-15-12667-2015

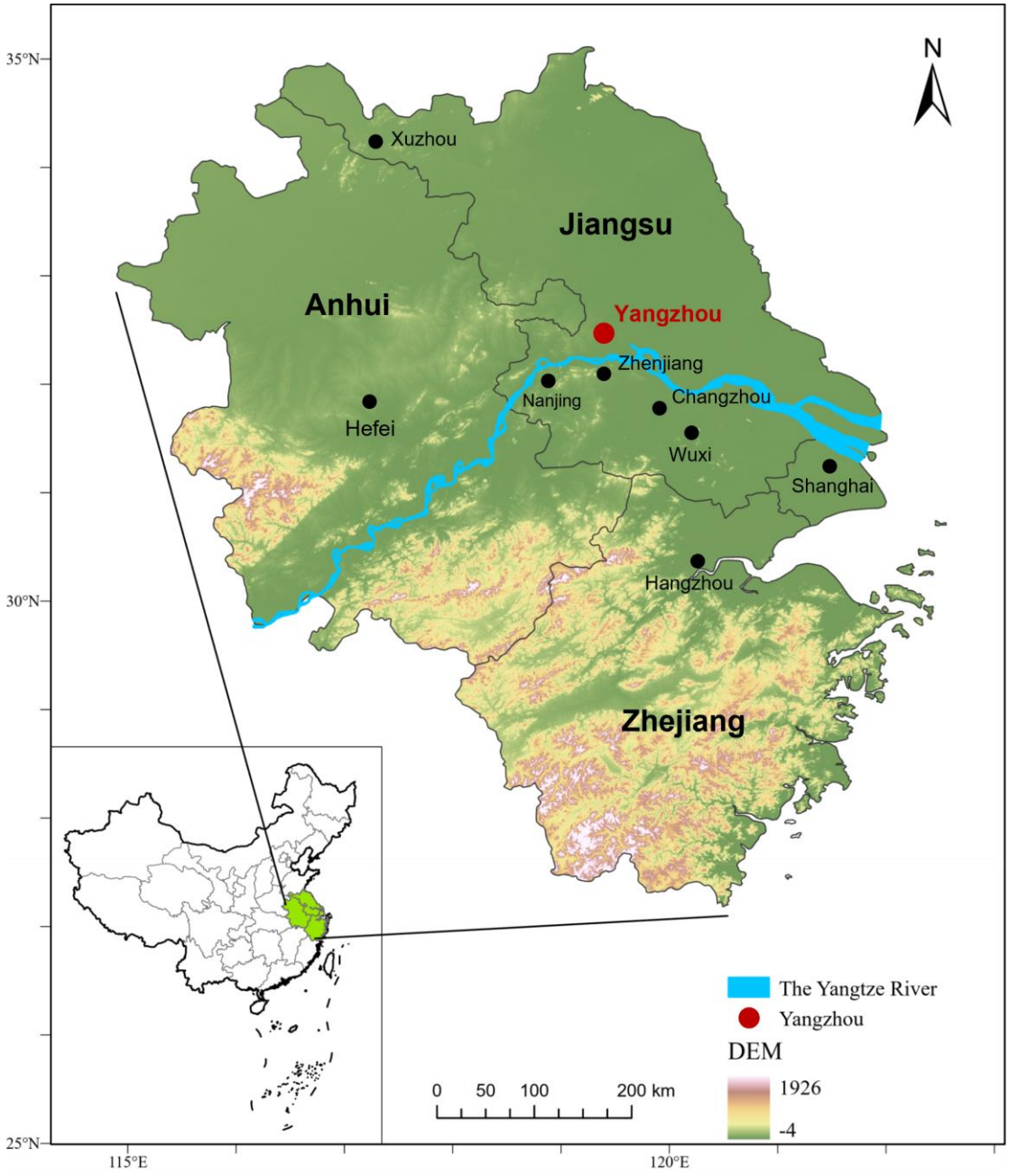

Figure 1. Geographical overview of the Yangtze River Delta (YRD) Region in China, depicting the major cities within the YRD and the sampling site located in Yangzhou. The color gradient from green to white indicates varying altitudes across the region (Maps were generated by using ArcGIS Pro).

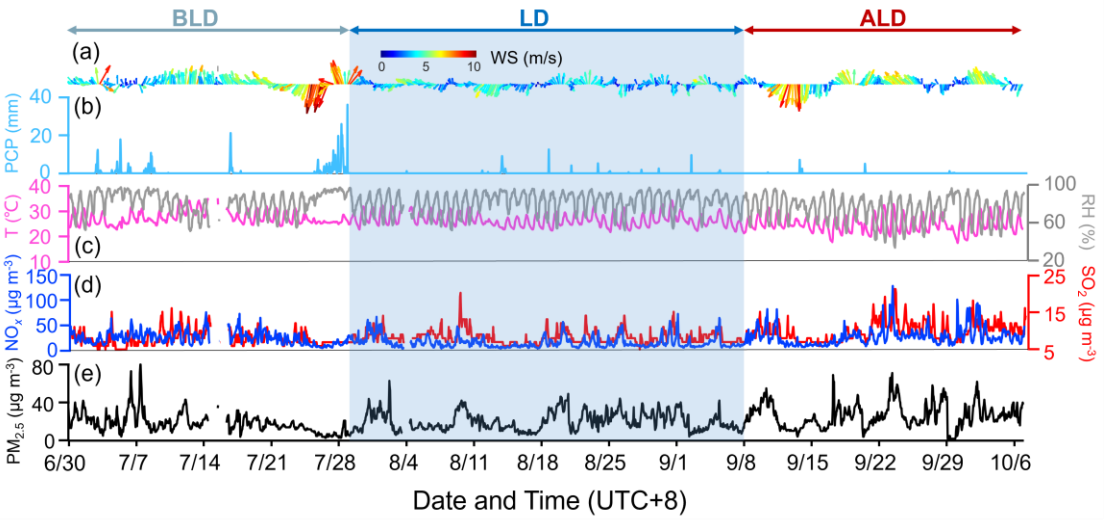

946

947 **Figure 2.** Temporal variations of **(a)** wind direction (WD) and wind speed (WS), **(b)**
948 precipitation (PCP), **(c)** temperature (T) and relative humidity (RH), **(d)** concentrations
949 of NO_x and SO_2, and **(e)** mass loading of $PM_{2.5}$. The grey, blue, and red arrow ranges
950 denote the periods before lockdown (BLD), during lockdown (LD), and after lockdown
951 (ALD).

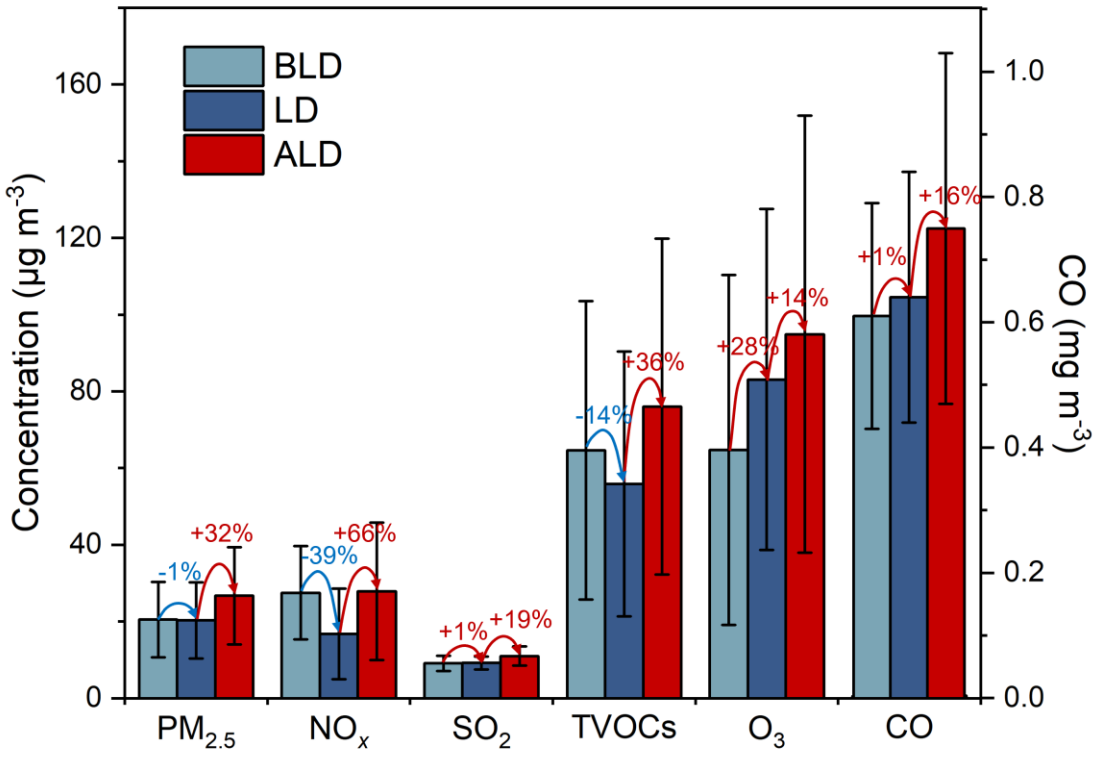

952

953 **Figure 3.** Ground-based observations of $PM_{2.5}$, NO_x, SO_2, O_3, CO, and TVOC
954 concentrations in Yangzhou. The figure compares the averages during the BLD (grey),
955 LD (blue), and ALD (red) periods. Error bars indicate SDs over different lockdown
956 periods.

957

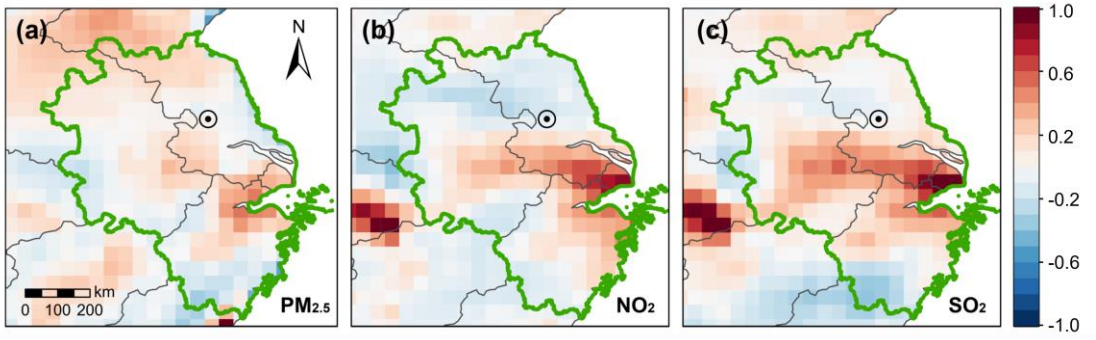

Figure 4. The fractional changes (i.e., (LD – BLD)/BLD) of **(a)** $PM_{2.5}$, **(b)** NO_2, and **(c)** SO_2 between BLD and LD periods based on spaceborne measurement. The circle symbols in the maps indicate the location of Yangzhou, and the green region represents the YRD.

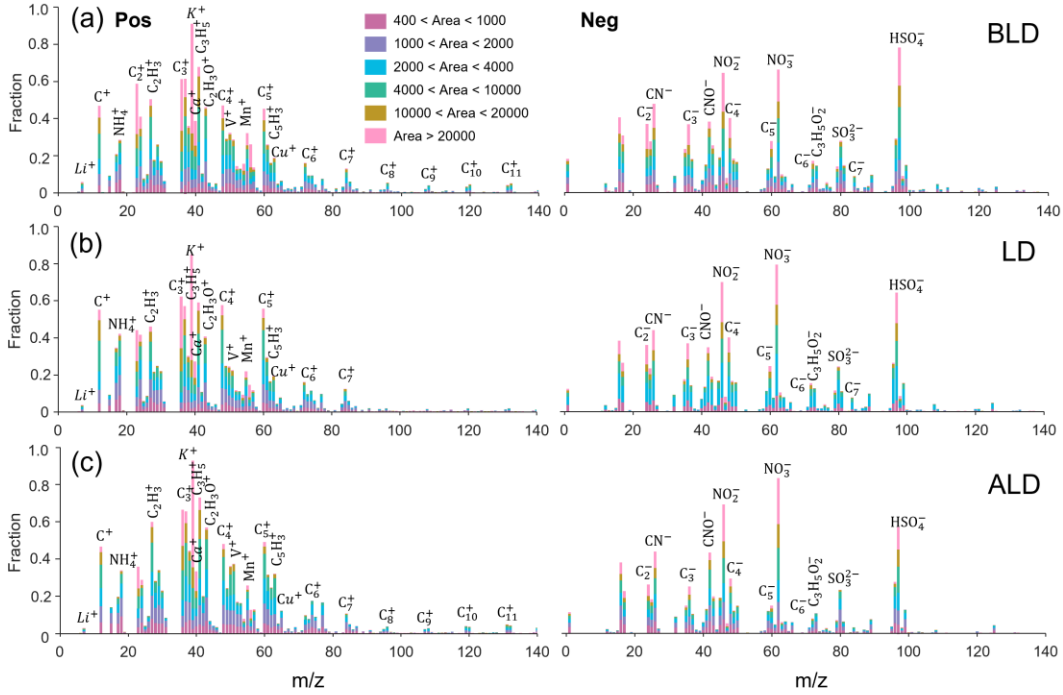

Figure 5. The average positive and negative mass spectra of BCc **(a)** before the lockdown period (BLD), **(b)** during the lockdown period (LD), and **(c)** after the lockdown period (ALD).

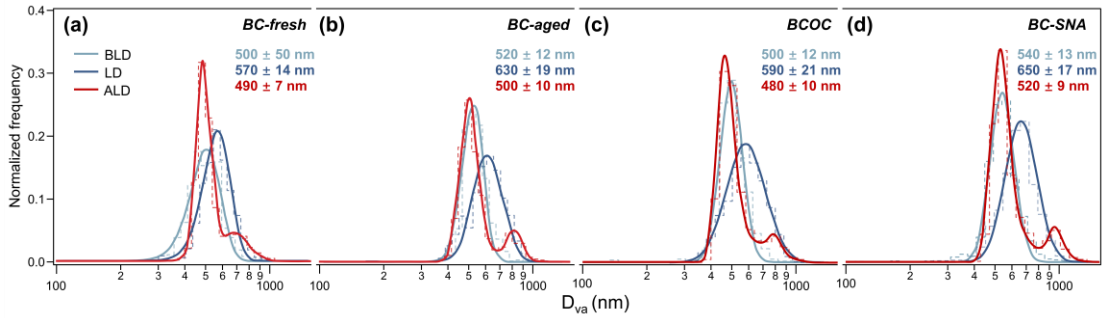

968

969 **Figure 6.** Size distribution of different types of BCc during different periods in
970 Yangzhou. **(a)** BC-fresh particles, **(b)** BC-aged particles, **(c)** BCOC particles, and **(d)**
971 BC-SNA particles. The Log-normal distribution was used to fit the unimodal size
972 distribution, and the Lorentz distribution was used to fit the bimodal size distribution.
973 The corresponding mode sizes (with the standard deviations) are also shown.

974

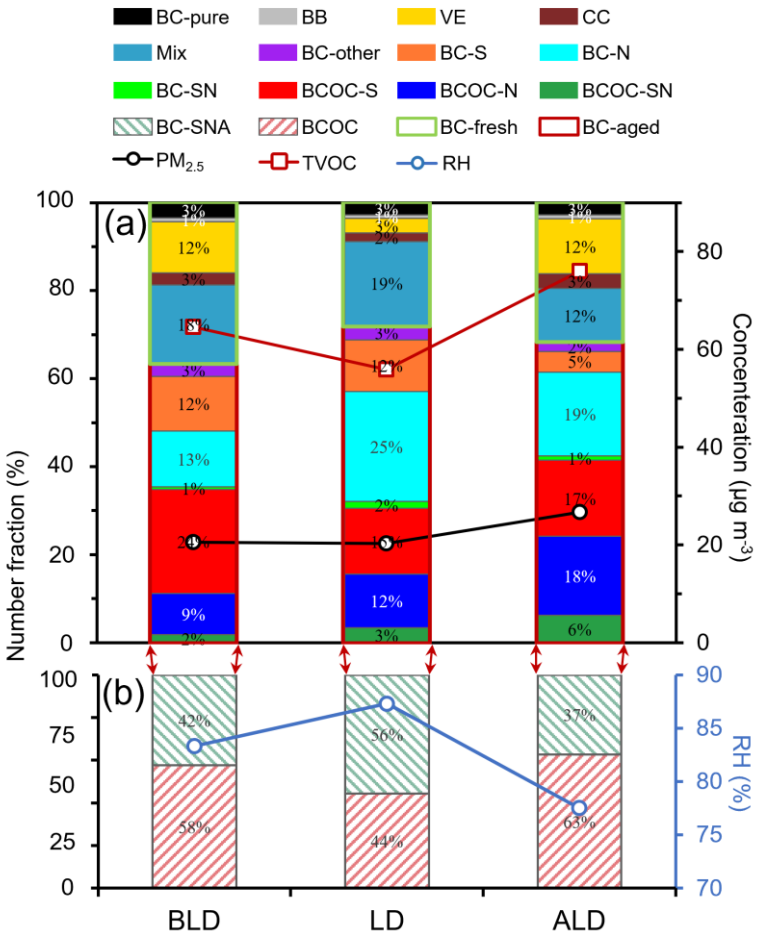

975

976 **Figure 7.** Number fractions of BCc. **(a)** The number fractions of different BCc along
977 with the concentrations of $PM_{2.5}$ and total volatile organic compounds (TVOC). **(b)** The

number fractions of different types of BC-aged particles along with relative humidity (RH).

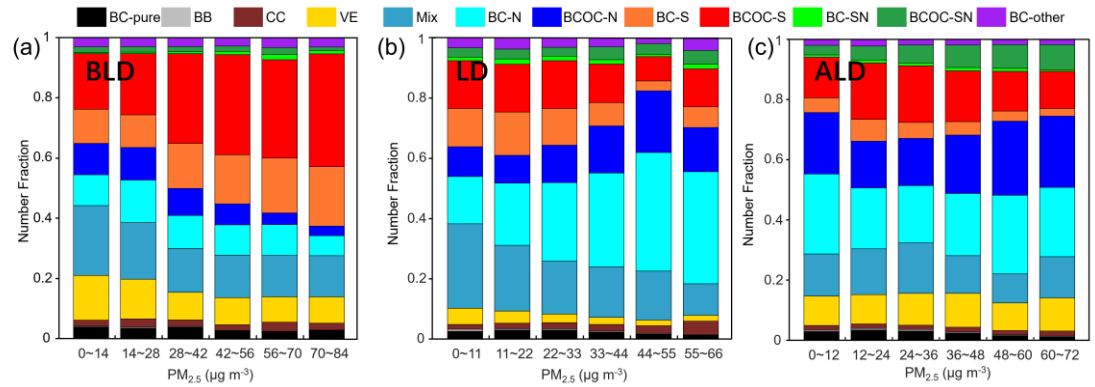

Figure 8. Variations of number fractions of BCc particle types with $PM_{2.5}$ mass concentrations during **(a)** the BLD period, **(b)** LD, and **(c)** the ALD period.

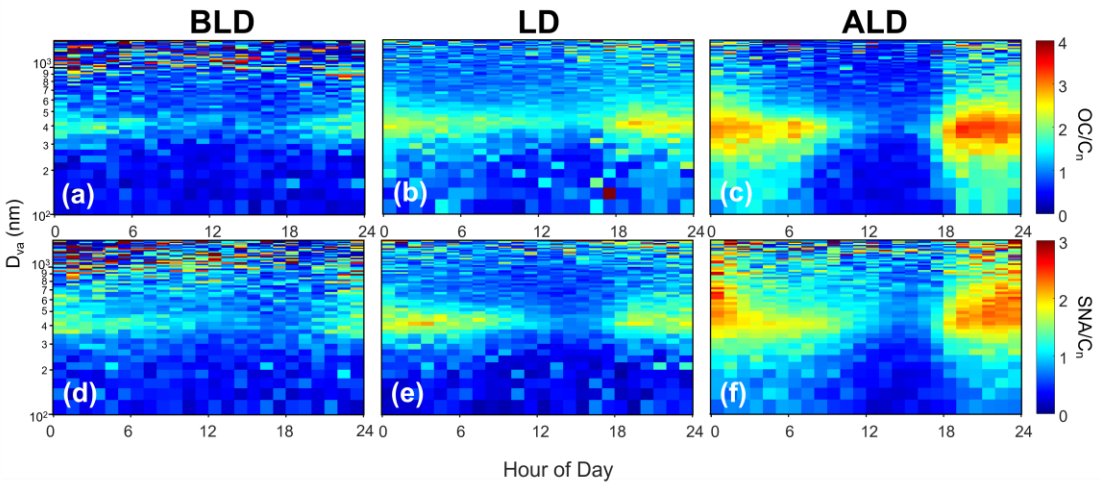

Figure 9. Diurnal variations of the ratios of OC/Cn and SNA/Cn with a size distribution of BCc during **(a, d)** BLD, **(b, e)** LD, and **(c, f)** ALD.

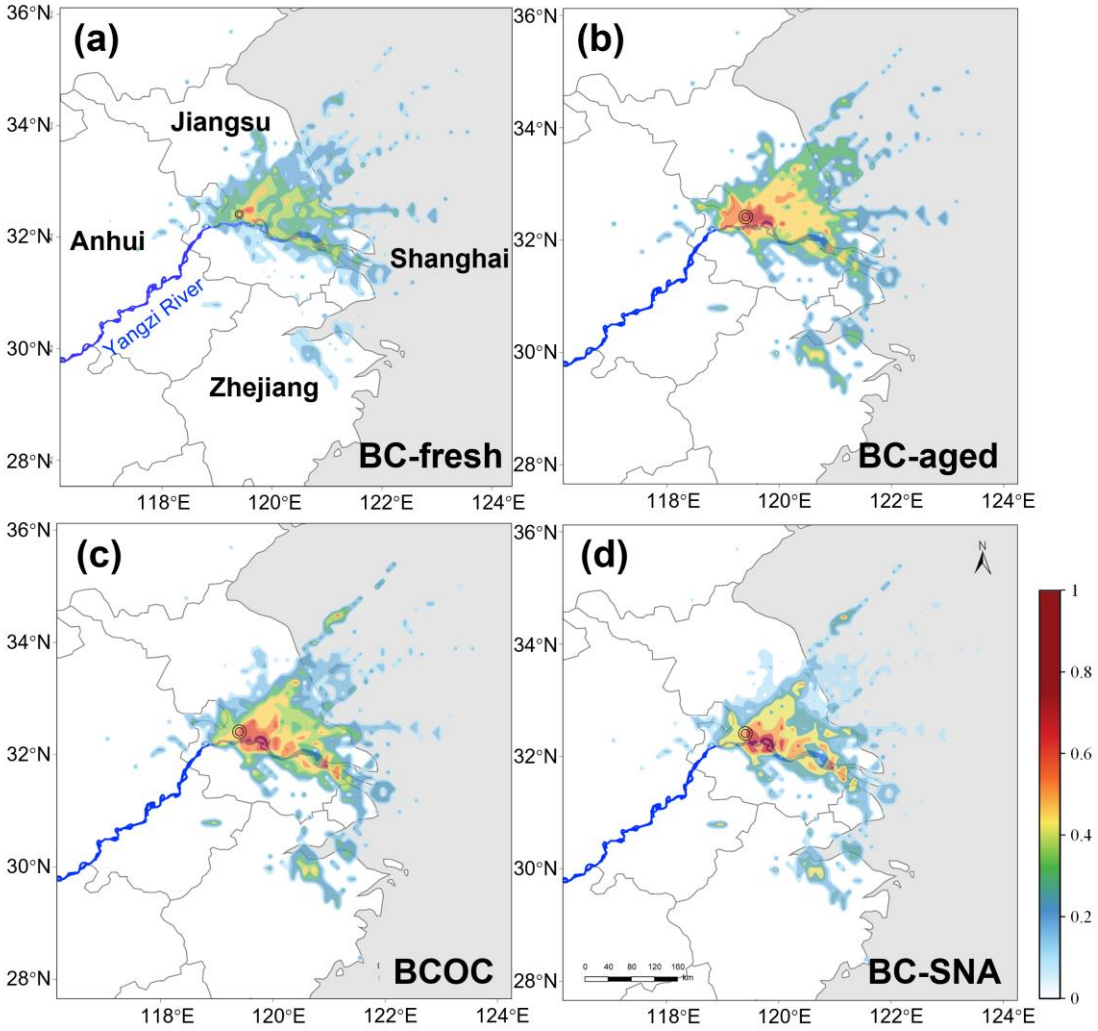

987

988 **Figure 10.** The PSCF maps for different BCc during LD. **(a)** BC-fresh. **(b)** BC-aged.
989 **(c)** BCOC. **(d)** BC-SNA.
990